SCIENCE CHINA
Physics, Mechanics & Astronomy

• Review •
Progress of Projects Supported by NSFC · Spintronics

January 2013 Vol.56 No.1: 70–84
doi: 10.1007/s11433-012-4975-3

Thickness-driven spin reorientation transition in ultrathin films

MIAO BingFeng[1], MILLEV YonkoTimtchev[2], SUN Liang[1], YOU Biao[1], ZHANG Wei[1] & DING HaiFeng[1*]

[1] *National Laboratory of Solid State Microstructures and Department of Physics, Nanjing University, 22 Hankou Rd., Nanjing 210093, China;*
[2] *American Physical Society, 1 Research Road, Ridge, New York, USA*

Received November 27, 2012; accepted December 11, 2012; published online December 26, 2012

We review recent studies by different experimental means of ultrathin films, exhibiting thickness-driven spin reorientation transitions (SRTs). The stage is set by determining, via phenomenological thermodynamic description, of the relevant phase diagrams for the possible types of SRT with and without applied magnetic field. Suitable representation may be chosen such that best use is made of the linear character (under thickness variation) of the system's path in anisotropy space. The latter involves higher-order bulk and surface anisotropies in a substantial way. We examine sensitive experimental techniques for the detection and quantification of SRTs, such as hysteresis measurements with magneto-optical Kerr effect (MOKE), micromagnetic studies utilizing scanning electron microscopy with polarization analysis (SEMPA), photoemission electron microscopy (PEEM) and spin-polarized low-energy electron microscopy (SPLEEM) as well as *ac* magnetic susceptibility measurements via MOKE. Key issues are conclusively discussed including the identification of reliable experimental fingerprints about whether a given SRT proceeds via a phase of coexistence or via a cone (canted) phase. We demonstrate how the application of the general theoretical ideas to carefully designed measurements leads to the determination of the most important material parameters in any ultrathin-film SRT, namely, the surface (interface) magnetic anisotropy constants. The review concludes by our personal outline for future promising work on SRTs.

ultrathin magnetic films, spin reorientation transitions, magnetic anisotropy

PACS number(s): 75.70.-i, 75.30.Gw, 75.30.Kz, 75.40.-s

Citation: Miao B F, Millev Y T, Sun L, et al. Thickness-driven spin reorientation transition in ultrathin films. Sci China-Phys Mech Astron, 2013, 56: 70–84, doi: 10.1007/s11433-012-4975-3

A spin reorientation transition (SRT) is, generally, a crossover between different states of macroscopic magnetic order (antiferromagnetic, canted, ferrimagnetic or ferromagnetic), which is effected through a rotation of the macroscopic magnetization into a new equilibrium direction under variation of experimentally controllable, or at least identifiable, parameters such as temperature, stress, film thickness, etc [1]. Whenever such variations affect the balance between competing and often subtle contributions to magnetic anisotropy, the energetically preferred axis of magnetization (spin axis) may change orientation. The study of SRTs in the bulk has a long history, mostly focused on the temperature-driven reorientations [2,3]. Recently, much of the progress in the study of magnetism and magnetic materials has been driven by the fundamental and practical interest to explore the meso- and nanoscales. Suffice it to mention the discovery and fast technological implementation of the giant magnetoresistance effect, which opened up the new field of spintronics [4–6]. Much of its proven and future capabilities, as well as those of ultra-dense magnetic data storage [3,7], depend crucially on the reliable control of the magnetization orientation in one or more thin or ultrathin magnetic layers of the sometimes rather intricate multilayer sandwich structures. Thus, having a clear and detailed un-

*Corresponding author (email: hfding@nju.edu.cn)

derstanding of reorientation processes in the ultrathin regime is bound to retain its high priority.

Given the vastness of the context, we will restrict our attention to the particular, yet broad and important enough, problem of thickness-driven SRTs in ultrathin magnetic films [8,9]. There, the magnetic stray field for perpendicularly oriented magnetization ***M*** is the maximal possible, hence, so are also the demagnetization effects. Yet another, quantitative way to state this is that the shape anisotropy for ***M*** along the perpendicular direction ***n*** is maximal, since the demagnetization factor along ***n*** is unity, immediately implying the two in-plane demagnetization factors are equal to zero as the sum of the three needs to be unity itself [10,11]. Hence, the magnetization in a sufficiently thin film would align within the film plane, if only the shape anisotropy was to be accounted for. However, the reality of the ultrathin limit is such that quite a few systems do exhibit macroscopic magnetization, perpendicular to the film plane. Clearly, a competitor more powerful than shape anisotropy must have entered the game and needs to be identified (see below). Upon increase of the film thickness, the magnetic easy axis of the system would rotate away from ***n*** and would end up in the plane to minimize the demagnetizing energy. This is precisely what a thickness-driven SRT is about. The reorientation process is of particular interest in studies and applications of perpendicular magnetic recording which can offer, in principle, a significant increase of the area density, compared to in-plane recording [12–14]. The thickness-driven SRT can be largely understood as due to the enhanced surface/interface magnetic anisotropy which becomes important or even dominant at sufficiently low film thicknesses. It is generally believed that the surface/interface magnetic anisotropy originates from the change of chemical bonding, which in turn derives, fundamentally, from the broken crystallographic symmetry at surfaces and interfaces, including quantum-chemical factors of prime importance like the coordination number of a magnetic ion etc. [15–18].

It has been found that the magnetic easy axis changes from perpendicular to in-plane with increasing film thickness for Fe/Cu(001) [19], Fe/Ag(001) [20,21], Fe/Au(001) [22], Co/Au(111) [13,23–27] systems. However, counterintuitive cases have also been detected as, for instance, the system Ni/Cu(001) which has a sharp transition from in-plane to perpendicular magnetization at about seven monolayers (ML) of thickness, followed by a gradual transition back to in-plane magnetization beginning at 37 MLs [28,29]. Interestingly, Co/Ru(0001) shows a similar behavior, yet within a narrow thickness window of only a few MLs [30]. In general, the SRT can proceed via a canted state of magnetization with a thickness-dependent variation of the canting angle or, alternatively, via a coexisting state, in which ***M*** may be oriented partially perpendicularly and partially in the plane, raising the question of possible domain formation and evolution. There have been differing reports on how and why the SRT unfolds in different systems, the Co/Au (111) system remaining a prime case of debate.

In this review, we will attempt to give an account of the salient features of thickness-driven SRTs, using a phenomenological coherent-rotation description of thermodynamic stability and discussing different relevant modern experimental techniques and examples. Our approach allows, among other things, to identify and determine quantitatively the values of the surface/interface constants beyond the lowest order in magnetic anisotropy. The knowledge of those is paramount for successful anisotropy engineering in spintronics device design. Studies of magnetic susceptibility emerge as a most promising tool to unravel the SRT mysteries.

1 Phenomenological description

1.1 Spin reorientation transition in zero field

When the in-plane anisotropy of the film is negligible, the angle-dependent free energy density f_A for an ultrathin film is given by

$$f_A = \tilde{K}_1 \sin^2(\theta) + K_2 \sin^4(\theta). \quad (1)$$

Here, $\tilde{K}_1$ and K_2 are the first- and second-order anisotropy constants, which generally depend on thickness and temperature, while θ is the angle between the surface normal ***n*** and the direction of ***M***. The influence of shape anisotropy is included in $\tilde{K}_1$ as:

$$\tilde{K}_1 = K_1 - \frac{1}{2}\mu_0 M^2. \quad (2)$$

The phase diagram has been discussed in detail by Millev et al. [31,32]. The essence of the analysis is as follows. Minimization of the free energy with respect to θ yields three solutions for the equilibrium angle $\sin^2(\theta_{eq})$=0, 1 and $-\tilde{K}_1 / K_2$, corresponding to vertical, in-plane, and canted phases, respectively. The vertical phase is stable for $\tilde{K}_1 > 0$, the in-plane phase is stable for $K_2 < -\tilde{K}_1 / 2$, and the canted phase for $\tilde{K}_1 < 0$ and $K_2 > -\tilde{K}_1 / 2$ (see Figure 1). Arguably, the most interesting part of the phase diagram is the region where the vertical and in-plane phases may coexist. It is located in the fourth quadrant, with $\tilde{K}_1 = 0$ and $K_2 = -\tilde{K}_1 / 2$ as the two boundaries. Plots of typical angle-dependent energies for the four regions are given as inserts in Figure 1 and illustrate amply the fact that, for the vertical and in-plane regions, the angle-dependent energy plots have only one energy minimum at 0° and 90°, respectively, and the same is true for the canted state where the only energy minimum exists for an angle between 0° and 90°. In contrast, within the coexistent part of the diagram

the energy features two local minima, one at 0° and the other at 90°. The region of coexistence can be divided into two sub-regions with a boundary $K_2 = -\tilde{K}_1$, defined as the line where the vertical and the in-plane configuration have equal energies, that is, their corresponding local minima are equally deep, hence, the barrier separating them is equally high when seen from either minimum. On each side of this boundary, it is one or the other configuration which is energetically more favorable, and this is seen in the inserted energy plots in Figure 1.

The dependence of K_i on the magnetic film thickness t creates the very possibility for a SRT, and the explicit form of this dependence is instrumental for a meaningful quantitative description of the thickness-driven SRT [see, however, the discussion related to eq. (6) below]. A widely accepted phenomenological Ansatz for the separation of volume and surface contributions was proposed by Gradmann [3,25,33],

$$K_i(t,T) = K_{ib}(T) + \frac{K_{is}(T)}{t}, \quad i = 1, 2, \tag{3}$$

where the subscript b stands for bulk and s stands for surface/interface contributions to K_1 and K_2. With the help of the concept of "anisotropy flow", driven by the thickness variation of the film [25,31,32], one can describe a SRT by plotting the trajectory $\{\tilde{K}_1(t,T), K_2(t,T)\}_{T=\text{constant}}$ in a $\tilde{K}_1 - K_2$ diagram. The usefulness of the flow concept is that the thickness-driven path is linear under rather general conditions beyond the 1/t dependence. As an immediate corollary of this linearity, one can identify from the diagram, essentially by inspection, three generic SRT possibilities, depending on the sign of K_2 at the transition. The transition from vertical to in-plane magnetization occurs via a continuous canting of $\boldsymbol{M}$ when K_2>0 (*e.g.* linear trajectory AD in Figure 1), or it directly changes from the vertical to the in-plane direction when K_2=0, which seldom happens in any real system. In this latter case, though, the absence of first- and second-order magnetic anisotropy may in itself provide an unique system to study even higher-order anisotropy or contributions from commonly neglected, weaker interactions such as the Dzyaloshinskii–Moriya interaction [34,35]. The third situation is for K_2<0, where the transition proceeds via a state of coexisting phases (see the linear trajectory EH in Figure 1).

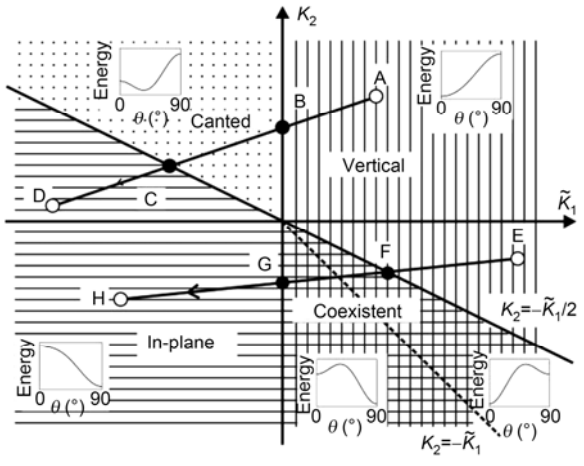

Figure 1 Phase diagram in anisotropy space. The inserts show a typical angle-dependent free energy in the respective part of the diagram. The linear paths AD and EH lead to thickness-driven SRT via a canted and coexistent state, respectively.

For the Co/Au(111) system, there has been a long debate about the type of the SRT. Each of the distinct nontrivial scenarios has been reported by different groups. Thus, for instance, a continuous rotation has been reported in refs. [23,36], while at the same time solid evidence has been provided for a thickness-driven SRT which proceeds via the coexistence part of the phase diagram [25,26]. Further below in this review we will spend some time to discuss reliable criteria for the identification of the type of the SRT in a consistent manner.

1.2 Spin reorientation transition in external field

The application of external magnetic field to a system with a SRT is duly taken into account by including the Zeeman term in the relevant thermodynamic potential density. Thus, instead of eq. (1), one employs

$$\begin{aligned} g_A &= \tilde{K}_1 \sin^2(\theta) + K_2 \sin^4(\theta) - \boldsymbol{H}\cdot\boldsymbol{M} \\ &= \tilde{K}_1 \sin^2(\theta) + K_2 \sin^4(\theta) - HM\cos(\theta - \phi), \end{aligned} \tag{4}$$

where ϕ is the angle between $\boldsymbol{H}$ and the normal to the surface $\boldsymbol{n}$.

Within the coherent rotation approximation and for a fixed direction of the field (ϕ=const), the conditions for the existence and stability of the possible phases are the same as without field, $\frac{\mathrm{d}g_A}{\mathrm{d}\theta} = 0$, $\frac{\mathrm{d}^2 g_A}{\mathrm{d}\theta^2} \geqslant 0$, yet there is now one more physical parameter to worry about. There are more than one orderly ways to keep track of the ensuing phase diagrams. Three generic and appealing representations have been explored in sufficient detail already, as have been also the mapping transformations between any possible set of variables [25,37,38]. The representation which has been found especially useful in the context of SRT in thin magnetic films comes about by casting the anisotropy energy density in a dimensionless form through normalization with respect to the Zeeman amplitude HM:

$$\tilde{g}_A = g_A / HM = \alpha \sin^2(\theta) + \beta \sin^4(\theta) - \cos(\theta - \phi), \tag{5}$$

where now $\alpha = \tilde{K}_1 / HM$, $\beta = K_2 / HM$. What makes this (α, β) representation so special in the context of SRTs in ultrathin films is that the thickness-driven trajectories, representing the evolution of the system, are linear under conditions, much more general than the usual 1/t-dependence of the interface anisotropy. To see this, consider a generalized

form of eq. (3) of sect. 1.1 where the additive thickness-dependent surface contribution is given by some functions $f_i(t)$ (i = 1,2) with the temperature dependence suppressed. As long as the functions $f_1(t)$ and $f_2(t)$ are of the same functional form, with the case $f_1(t)=f_2(t)=1/t$ being just one particular possibility, the thickness dependence can be eliminated to give

$$K_2 = s\tilde{K}_1 + p, \tag{6}$$

where the slope s and the intercept p depend on the material parameters of the system, but not on the thickness [37]. Obviously, normalization with respect to the Zeeman amplitude does not change the linear character of the trajectory under the same general assumptions and with the same slope and intercept as for the field-free case.

The spectacular usefulness of the (α, β) representation is also evident in the following very general features. Working out the details of the simple elimination of thickness above, the slope of any linear trajectory is equal to the ratio of the surface anisotropies only, $s=K_{2s}/K_{1s}$, hence, independent of the applied field. As an immediate consequence, the linear trajectories, corresponding to different applied fields, are parallel to each other. From the same simple calculation, the *sign* of the intercept p is independent of the field, while its magnitude is inversely proportional to the field. As already noticed in ref. [37], these rather general features of the (α, β) representation can be succinctly summarized by stating that: (i) the isolines of constant field are nothing but the family of parallel segments which connect the start and finish of the system's evolution under the SRT; these linear segments are the possible thickness-driven trajectories that the system would follow; (ii) the isolines of constant thickness are nothing but the family of straight rays, flowing into the origin with increasing field. The situation is illustrated in Figure 2, where the (α, β)-diagram is given for the case when the magnetic field is applied perpendicularly to the easy axis. It is rather enlightening to realize that what is specific here are the phase boundaries (thick lines), while for a given set of material parameters the paths of evolution $\{A_\mu, B_\mu\}$ are invariant.

The most experimentally relevant cases of applied field are with field along the normal to the film, $H_\perp$, and with field in the plane, $H_=$. (These two field configurations have also been labeled as H_n and H_p, respectively.) Quite generally, the magnetic field leaves only two possible phases, namely, one in which the external field plus the anisotropy fields of first and second order drive $\boldsymbol{M}$ to align with $\boldsymbol{H}$ (conforming phase) and one in which the competing fields settle on having $\boldsymbol{M}$ canted with respect to $\boldsymbol{H}$ (canted or cone phase). Depending on which experimental situation is explored, the conforming phase would be either in-plane conforming or perpendicular conforming. Beyond these general observations, one does need to carry out detailed stability analysis as outlined at the beginning of this section, keeping an eye on the fate of the field-free phases. Surrendering one degree of generality, the cases of positive (β>0) or negative (β<0) second-order anisotropy emerge as distinct. In the first case and for any of the two field orientations, there are two phases, canted and conforming, which are separated by a linear boundary. In the second case, there are three possible phases: canted, conforming, and a phase, where canted and conforming states coexist. Thus, one of the most interesting possibilities, the coexistence phenomenon, survives the application of external field, albeit in a modified form, whereby (i) the coexisting phases are not out of plane and in the plane, and (ii) one of the phase boundaries is nonlinear (cubic parabola) [38].

As in the field-free case, the SRT-related effects are most pronounced at the most interesting points in the phase diagram, the crossing points of the linear thickness-driven flow with the phase boundaries. Later in this article, most of the relevant features of the crossover points are brought to bear on the analysis of susceptibility measurements. Suffice it to state here that the detailed quantitative knowledge of the phase diagram, combined with the natural idea of tracking the evolution of the system by means of its thickness-driven path, provides an overview of all possible scenarios which may unfold depending on the specific material parameters at play in one or other thin-film magnet. Thus, quite generally a system with a SRT may have one, two, or three crossover points. To our knowledge, the latter possibility has not yet been observed, but this may have just been due to the fact

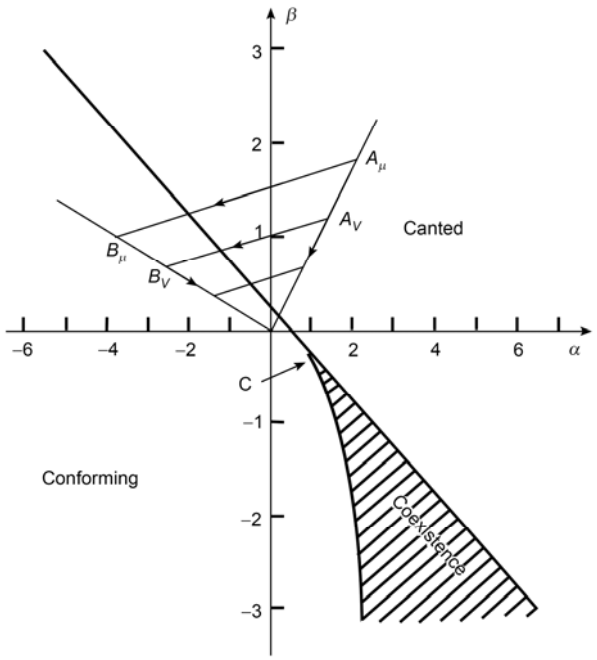

Figure 2 Linear trajectories between initial $\{A_\mu\}$ and final $\{B_\mu\}$ states for thickness-driven reorientations. In the (α, β) phase diagram, this linearity is preserved for any orientation of the applied field. Taken from Millev et al. [37]. Reprinted with permission from IOP.

that it has not been anticipated. An even more exotic behavior might ensue for the case when the path of the system is tangent to the cubic parabola; the implications of such a limiting case have not been explored either. The situation is illustrated in the (α, β)-diagram in Figure 3 for the in-plane field configuration, where the grey region is the coexistence domain, traversed by the segment (η, ζ) along which the system evolves. The crossover points are X_L and X_N with the subscripts deliberately chosen to indicate linear (L) and nonlinear (N) phase boundary crossings, respectively. In practice (that is, for any particular system with a SRT), the X-points lead to the straightforward identification of the respective critical thicknesses where a SRT occurs; t_L or t_N would then denote the critical thickness, related to a linear or nonlinear phase boundary, respectively. In essence, the identification of the crossover points- and, hence, of the critical thicknesses-amounts to a plane-geometric specification of the points where a curve (the trajectory) crosses two other curves (the phase boundaries), all curves being explicitly known from thermodynamic stability analysis [38].

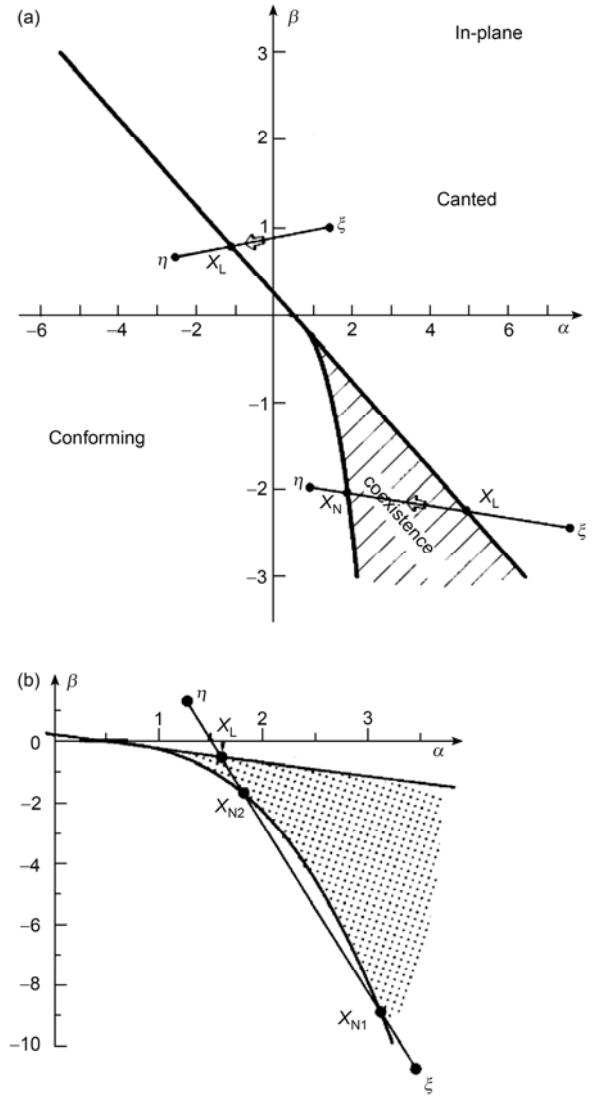

Figure 3 Possible scenarios for thickness-driven transitions according to the number of crossing points X of the linear path (η, ζ) with the phase boundaries of the system (in-plane configuration). X_L (X_N) are the crossing points with a linear (nonlinear) boundary, respectively. One, two, or three SRTs are possible. (a) Systems with one or two thickness-driven SRTs; (b) Systems with three SRTs. Taken from Millev et al. [38] Reprinted with permission from APS.

2 Hysteresis studies of SRTs

Magnetic hysteresis is a relatively straightforward feature that is sensitive, hence, gives access, to the magnitude of magnetic anisotropy in a magnetic system. Hysteresis measurements have been widely applied to systems with both temperature-driven [19,21,39] and thickness-driven SRTs [22,23,27]. In ultrathin films, the hysteresis-related signals are very weak, which is why techniques with high sensitivity like those implementing the magneto-optical Kerr effect (MOKE) [40,41], superconducting quantum interference devices (SQUID), or X-ray circular dichroism (XMCD) are the state of the art. Here, we choose to focus on MOKE studies, since in comparison with the other techniques it is relatively cheap and easy to set up in the lab.

Within the coherent rotation model, one finds that the hysteresis process with the field along the easy axis exhibits a square loop, while the loop with field along the hard axis is negligibly thin and is a nearly reversible tilted line, leading to saturation. When there is a SRT, the shape of the hysteresis loop is modified significantly as the transition evolves with the thickness. In addition, one can also judge which axis is the easy one by simply comparing the hysteresis measurements along the different field directions.

Figure 4 presents a typical sample of such behavior. One can follow the MOKE loops, measured for successively varying Fe thickness on an Au(001) substrate with the magnetic field applied out of plane (polar geometry; left part of Figure 4), and in the plane (longitudinal geometry; right part of Figure 4). The ultrathin films were prepared by molecular beam epitaxy on a polished MgO(001) substrate under ultrahigh-vacuum (UHV) conditions [22]. In the polar geometry, the hysteresis loop at 2.0 MLs, with 1 Fe ML equivalent to 1.435 Å, exhibits an almost square loop, *i.e.*, a typical easy-axis loop. On the other hand, the loops are of the hard-axis, tilted-line variety for Fe thicknesses above 2.3 MLs, suggesting that a SRT occurs between 2.0–2.3 MLs. One can also observe that the slope of the tilted line decreases, while the saturation field increases, which originates in the thickness variation of the anisotropy constant. The detection of the SRT is confirmed further by comparison with the in-plane loops shown on the right in Figure 4, which evolve in an opposite way, namely, having an almost square easy-axis loop at and above 2.3 MLs and a typical hard-axis loop at 2.0 MLs.

In the course of the spin reorientation transition, the magnetization typically contains both vertical and in-plane

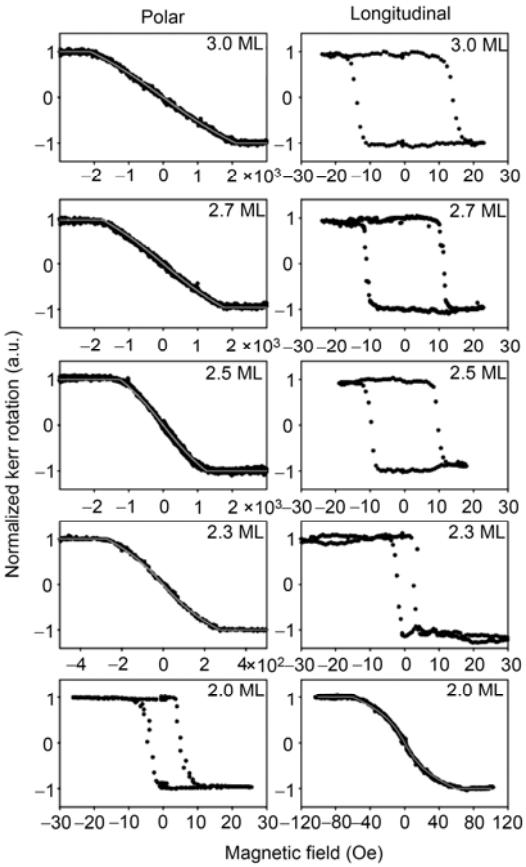

Figure 4 Polar and longitudinal MOKE loops measured across the range of the SRT for successive Fe thickness between 3.0 and 2.0 ML for Fe/Au(001). The hard-axis loops are given together with the corresponding simulated curves. Taken from Wilgocka-Ślęzak et al. [22]. Reprinted with permission from APS.

components. A MOKE measurement will detect both components even if it has been divided into three geometries, i.e., polar, longitudinal, and transverse geometries according to the relative arrangement of the magnetization orientation and the scattering plane of the incident light [40,41]. The mixing of the polar and longitudinal Kerr effect sometimes makes the results difficult to interpret. For instance, in the study of the temperature-driven SRT of Fe/Ag(100), Qiu et al. reported a sign change and a significant increase of the magnitude of the Kerr signal, obtained with in-plane field geometry [21]. The authors attributed this phenomenon to the mixing of the polar and longitudinal signals.

To separate the mixing signal and obtain the pure polar/longitudinal signals, Ding et al. [42] proposed an experimental method, based on the different symmetries of the polar and longitudinal signals. To a first-order approximation the Kerr signal is a function of the direction cosine between the propagation vector of the incident light $\hat{\boldsymbol{k}}$ and the direction of the magnetization $\hat{\boldsymbol{M}}$, i.e., $\hat{\boldsymbol{k}} \cdot \hat{\boldsymbol{M}}$ [40]. In polar geometry the angles between $\hat{\boldsymbol{k}}$ and $\hat{\boldsymbol{M}}$ are exactly the same for inverted geometries. Hence, the polar Kerr signal is an even function of the angle of incidence. Exactly the same hysteresis loops have to be obtained in both geometries. On the contrary, in the longitudinal geometry the two angles between $\hat{\boldsymbol{k}}$ and $\hat{\boldsymbol{M}}$ are supplementary to those in the reversed experiment. This means that the longitudinal signal is an odd function of the incident angle. It will change sign if incident and scattered beams are interchanged. These basic symmetry properties are used to disentangle the mixed Kerr signals which may occur in a general geometry. Thus, by implementing two measurements of the Kerr signal in reversed geometries one can obtain the sum and difference of the polar and longitudinal Kerr signals. This allows one to determine the individual contributions: (i) by taking the sum of both signals one obtains twice the polar Kerr ellipticity, and (ii) by taking the difference one obtains twice the longitudinal Kerr ellipticity. The procedure has proven to be well-suited to separate the response of the longitudinal and polar Kerr effects [42].

Figures 5(a) and (b) present the hysteresis loops obtained with an angle of incidence of ±45° for ~5 MLs of Co on Au(111), which is close to the SRT region. The film was annealed at 470 K for 20 min and it was expected that it was covered by a thin layer of gold. The magnetic field was applied parallel to the film plane and the scattering plane of the light. A slight misalignment of 1–2° with respect to the surface plane could not be eliminated. The signals in the two measurements were quite different, depending on the relative orientation of the light and the external field. The two loops were inverted and their shape and magnitude differed quite strongly. If the magnetization was solely in the plane, a pure longitudinal Kerr signal with two identical, yet reversed loops would have been found. Following the procedure outlined above, the point-by-point difference and sum of the two curves were calculated. The results, divided

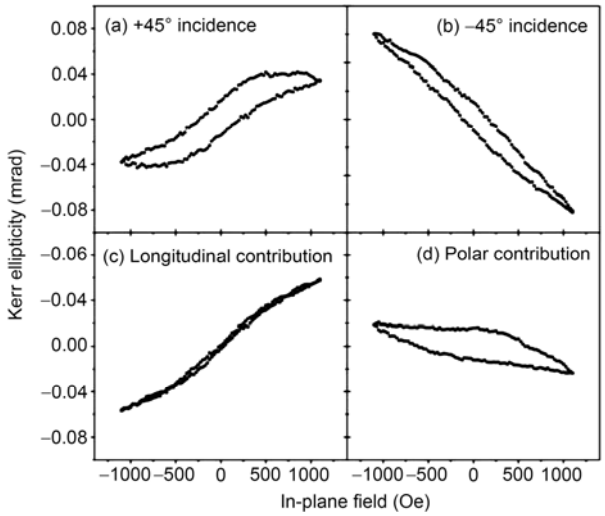

Figure 5 Kerr ellipticities for a Co film on Au(1 1 1) at a thickness close to the SRT. S-polarized light is impinging along +45° (a) and −45° (b). Panels (c) and (d) present the calculated longitudinal and polar contribution, using the data from (a) and (b), respectively. Taken from ref. [42]. Reprinted with permission from Elesvier.

by two, are shown in Figure 5(c) (difference) and Figure 5 (d) (sum), which are thus the extracted hysteresis loops for the in-plane and polar Kerr signals, respectively. One can see that the resulting pure in-plane signal is a typical hard-axis hysteresis loop, which is consistent with the square loop obtained in perpendicular field [42]. Rotating the optical plane with respect to the sample and the applied field direction by 90° and repeating the same procedure as described above, the magnetic components along the third orthogonal direction may also be measured. The magnetization components along all different directions can be quantified through additional calibration of the MOKE sensitivity in different geometries [26].

Recall that three different types of SRT were described above, contingent on the sign of K_2 at the transition. Can one use the hysteresis loop to identify the type of the transition in the real system? Figure 6 presents the answer to this question. There, panels (a)–(c) show the normalized magnetization components as functions of the in-plane field along the *x*-direction for a Co film on Au(11). The thickness of the film is 5.3±0.3 MLs. The magnetization has all three components in the whole field range when the field is applied in the *x*-direction, confirming that the system is indeed inside the SRT region. The *x*-component increases with increasing field, while the other two components initially increase with field but then decrease in even higher fields. When the field is applied along the z-axis, the hysteresis loop (Figure 6(d)) exhibits an almost square loop with full remanence. As shown in Figure 1, the canted state has only one energy minimum which is located at an oblique angle. The coexisting state has two energy minima at 0° and 90°. In the absence of magnetic field, the canted state can not be stabilized at 0° or 90°. Only in the case of a coexisting state, the film can be stabilized at either these two specific configurations or a combination of them. Therefore, the finding of full remanence confirms that the transition is via a coexistent state. One may ask why there is no full remanence found with the field aligned along the *x*-axis. This is because the magnetization is not fully saturated as is clearly seen in Figure 6(a).

From the hysteresis loop measurements one could also estimate the magnetic anisotropy constants. Moreover, in a varied-thickness experiment one can evaluate the surface/interface anisotropy constants under the widely accepted assumption, given in eq. (3). Other experimental techniques, such as, e.g., ferromagnetic resonance (FMR), are needed when further quantitative information for specific films is required [14,43].

3 Microscopic studies of SRTs

Spin-sensitive microscopic techniques, such as scanning electron microscopy with polarization analysis (SEMPA) [23–25], spin-polarized low-energy electron microscopy (SPLEEM) [44] and photoemission electron microscopy (PEEM) [45], are capable of analyzing directly both the orientation and magnitude of surface magnetization. Hence, spin-sensitive surface microscopy offers specific advantages in accessing information about SRTs. The above-mentioned techniques have been widely used in studying magnetic properties of various materials during recent years. For a recent review about state-of-the-art magnetic imaging techniques, the reader is referred to ref. [46]; see also refs. [47, 48].

Utilizing SEMPA, Allenspach et al. studied the thickness dependent SRT of epitaxially grown Co on Au(111). Figure 7 presents thickness-dependent magnetic images of essentially the same sample area. Increasing the thickness, the contrast of out-of-plane components (upper panel) decreases and almost disappears at 6 MLs. The in-plane components with sensitivity along the length of the page (lower panel), however, features the opposite trend. By comparing both panels, the SRT crossover region is identified to be between 4–4.5 MLs. With the assistance of additional measurements of the third component of $\boldsymbol{M}$, the authors were able to reconstruct the magnetization vector of individual pixels. They averaged them to obtain the average canting angle between $\boldsymbol{n}$ and $\boldsymbol{M}$, and concluded that a continuous crossover from out-of-pane to in-plane magnetization occurs within a finite thickness range of about 2 MLs; this was interpreted as a SRT along a path, like AD in Figure 1 above, via the canted-phase portion of the phase diagram. However, the same experimental observations as those just described would result if the SRT crossover were across the region of coexistence, like EH in Figure 1. This implies that additional independent information is needed to resolve the issue.

Oepen et al. [25] revisited the SRT of Co/Au(111) but on a wedge-shaped sample. Figures 8(b) and (c) present the vertical and in-plane magnetization configurations of Co/Au (111) wedge sample in the range of thicknesses between 3 and 6 MLs. The film was slightly annealed to improve the morphology, hence, it contained a thin capping layer of Au. Due to the enhanced interface anisotropy (two contributing Co/Au interfaces instead of one for the case of no capping layer), the SRT occurs at a higher cobalt coverage than that reported in ref. [23]. There are large vertical domains at lower coverage below the SRT. Besides, the domain size significantly decreases when the coverage approaches the SRT region. The simultaneously taken in-plane image does not have sufficient contrast at low coverage, yet ample contrast at higher Co coverage. The domain size increases with thickness in surprisingly good agreement with theoretical predictions [49–52]. Interestingly, when the vertical and in-plane images are superposed onto one image [Figure 8(a)], there still remains a range of thicknesses which exhibits neither vertical, nor in-plane magnetic contrast. This "magnetic contrast catastrophe" may be related to the significant decrease of the domain size in the SRT region with

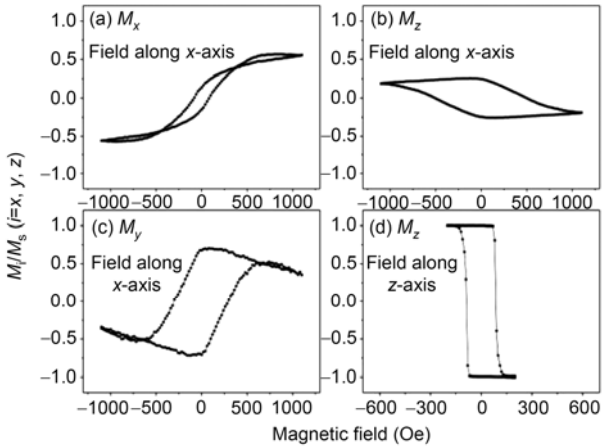

Figure 6 (a)–(c) The normalized magnetization components versus the in-plane field. The film thickness ((5.3±0.3)ML) was chosen to be within the region of the SRT. (d) The hysteresis loop obtained in a vertical field. Taken from ref. [26]. Reprinted with permission from APS.

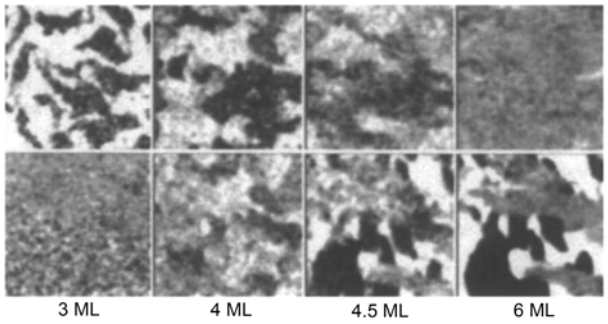

Figure 7 Magnetic domain images of Co/Au(111) thin films, showing the evolution of domain size and switching behavior as the Co film thickness is varied. Pictures taken at identical positions on the sample (within 2% of scan area) between evaporation of additional layers. At each thickness, the upper image gives the out-of-plane and the lower one - the in-plane magnetization component. Gray scale from black to white indicates the magnitude of the magnetization component along the axis of measurement; scan area 20×20 μm^2 [23]. Courtesy A, Allenspach, Zurich. Reprinted with permission from APS.

the domains becoming too small to be resolved by the employed instrument. After applying a perpendicular magnetic field, the vertical domain image at zero field [Figure 8(d)] pictures a single domain up to 5 MLs, which coincides with the higher thickness limit of the missing-contrast region. The finding of a single domain with full signal suggests a SRT which proceeds via a coexisting state, like along the line EH in Figure 1. If further annealing at 470 K is carried out, the vertical domain image, taken at room temperature, exhibits the single domain phase only up to 4.75 MLs [Figure 8(e)], suggesting magnetic domains are created above this thickness. That same thickness of 4.75 MLs is found to be the lower-thickness limit of the missing contrast region. The authors of ref. [25] identified these lower- and upper limits as the points F and G in the phase diagram shown in Figure 1. Following the theoretical analysis of sect. 1 above, one can easily deduce from the phase diagram that:

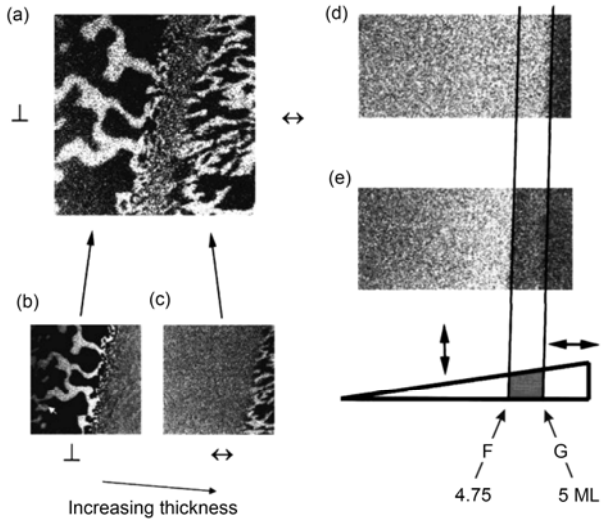

Figure 8 Domain structures of a wedged Co film on Au(111) in the thickness range through the reorientation obtained by SEMPA. (b) and (c) are obtained with out-of-plane and in-plane sensitivity, respectively (image size: 112.5 μm×112.5 μm). The Co thickness varies from 3 to 6 MLs with the direction indicated at the bottom. (a) is the combination image of (b) and (c). (d) Vertical domain structure after applying a perpendicular field. Image was taken at zero field with a size of 458.5 μm×217 μm. Thickness increases from left to right (3.6–5.2 MLs). (e) Vertical domain structure of the same area as in (d) but with further annealing at 470 K. Taken from Oepen et al. [25]. Reprinted with permission from APS.

$$\tilde{K}_1(t_F) + 2K_2(t_F) = 0, \quad \tilde{K}_1(t_G) = 0. \tag{7}$$

Building on this identification, the authors proposed an unified approach to evaluate the first-order and second-order magnetic surface anisotropy constants according to eqs. (3) and (7), assuming that bulk anisotropies are known. This resulted in the values of K_{1s}=8.0×10^{-4} J/m^2 and K_{2s}= −1.4×10^{-4} J/m^2 at room temperature for the system under discussion.

So far the discussion was mainly focused on the imaging of a state of coexisting phases. In the study of Co/Pt multilayers by means of SEMPA, the reorientation of magnetization from perpendicular to in-plane is found to happen via the state of canted magnetization. A stable domain pattern in the in-plane magnetization components is found for Co/Pt multilayers during the transition from an easy-axis to an easy-plane phase. Interestingly, the analysis of the domain pattern reveals that the magnetization canting is such that all in-plane orientations of magnetization are uniformly occupied. The authors concluded that the found structure was likely the cone state [53].

Vedmedenko et al. [54] carried out simulations of the spin texture inside a SRT domain for different types of transition by means of Monte Carlo simulations. Figure 9(a) presents the calculated magnetic domain structure for $\tilde{K}_1 = -0.4E_D$, $K_2 = 0.65E_D$, i.e., for values of the anisotropy constants, placing the system inside the canted phase, outlined in Figure 1. The spin texture is canted with domains neither fully perpendicular, nor fully in-plane. A rather in-

formative statistic, generated during the simulations, is shown in Figure 9(b)-the frequency distribution of magnetization, orientated in the *z*-direction. It shows that the magnetization is highly preferentially tilted with a canting angle of about 51° away from the plane of the surface, pointing either above or below that plane (the two peaks in the said figure). This is consistent with the existence of only one energy minimum in the phase diagram (see the corresponding one-minimum inset in Figure 1). The canting angle of $51° \approx \arcsin\sqrt{0.4/0.65}$ is also in good agreement with the energy minimum described in sect. 1.1. Since no in-plane anisotropy is included in the calculation, the in-plane component of magnetization varies with position and is directed in equiprobable directions. This prediction is resolved by Frömter et al. as the cone state just mentioned above [53].

Similar simulations for a coexisting phase [Figure 9(c), corresponding to $\tilde{K}_1 = E_D, K_2 = -0.8E_D$], however, show the magnetizations are either almost fully vertical or fully in-plane as also confirmed explicitly by the frequency statistic presented in Figure 9(d) [54]. The authors also found that the occupancies of vertical and in-plane domains depend on the ratio of $\tilde{K}_1 / K_2$. The average vertical component gradually changes from almost unity above $K_2 = -\tilde{K}_1/2$ to zero at $\tilde{K}_1 = 0$. This continuous change of the average magnetization component can lead to the erroneous conclusion that the reorientation proceeds via the canted phase of magnetization as described in the previous paragraph. The canted phase, however, does not exist in this part of the anisotropy space.

Moving on to another spin microscopy technique, we turn to spin-polarized low-energy electron microscopy (SPLEEM), which has the capability to image simultaneously domain structure and sample morphology in the vertical direction with high resolution when the imaging is taken on single crystalline samples. More precisely, the steps and the flat terraces can be distinguished due to the non-constructive and constructive electron beam interferences. In addition, the interference patterns of layers of different thickness could be different and allowed for thickness determination of individual islands on a single crystal surface [44]. The feature enables the study of the correlation between magnetic structure and morphology, the Holy Grail of solid-state magnetism.

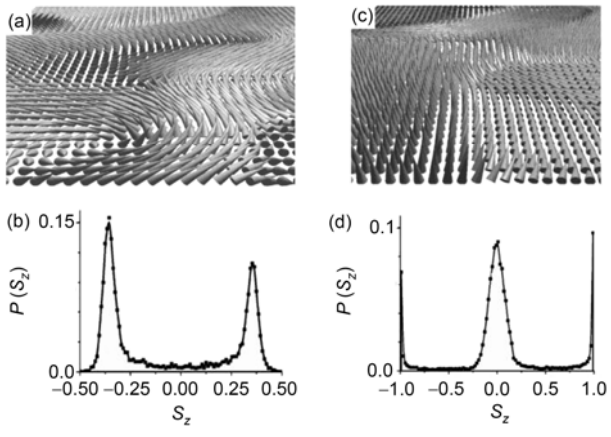

Figure 9 Micromagnetically generated spin texture with the respective frequency distribution of the magnetization orientation in the *z*-direction for a canted phase [(a) and (b)], and a coexisting phase [(c) and (d)]. The broadening of the peaks in (b) and (d) are due to a statistically small fraction of moments with non-optimal orientations caused by domain walls [54]. Reprinted with permission from APS.

Consider now Figure 10, which presents SPLEEM images of about 1.5 MLs of Co on a Ru(0001) substrate at 110 K [30]. The electron polarization is oriented: (a) out-of-plane; (b) in-plane and 13° off a compact direction; (c) in plane and 103° off a compact direction. The 2-ML islands are rendered in red and two small 3-ML islands are rendered in blue. The remaining area belongs to a single monolayer region. Based on the images shown in Figure 10(a)–(c), the magnetization orientation of each island is reconstructed and indicated by arrows (black and white arrows for out-of-plane, green arrows for in-plane). In comparison with the thickness of the islands, the authors of ref. [44] found that the magnetization in the 1-ML and 3-ML regions was in-plane, while only the magnetization at 2 MLs is oriented perpendicularly. The magnetization was confirmed to be in-plane for 3-ML or thicker Co films by imaging at higher thicknesses. This means that two sharp reorientation transitions occur at 1 ML and at 2 MLs, respectively. The first transition is associated with a structural transformation from laterally strained, pseudomorphic 1-ML thick films to relaxed 2-ML thick films. The authors identified, with the help of first-principle calculations, the combination of strain and additional interface or surface effects as the driving force for the perpendicular magnetization at 2 MLs.

Another interesting aspect of the thickness-driven SRT is the emergence of stripe domains when the thickness is approaches its critical value at the boundary of the SRT region [55–57]. Figure 11(a) presents the magnetic domain image of Fe(wedge)/Ni(5 ML)/Cu(001), obtained by PEEM. Only the in-plane domain is found above the transition region (2.7 MLs). Below the transition, the region with perpendicular magnetization shows a characteristic stripe-domain pattern [58]. The domain width decreases significantly when the thickness is approaching the crossover point at $t_{\mathrm{Fe}} \approx 2.7$ MLs. The domain structure cannot be resolved in the low-magnification image near the crossover point. However, a blown-up image [Figure 11(b)] does show clearly the persistence of the stripe domain structure down to very small scales. By plotting the domain width as a function of the Fe thickness, the authors find that the domain width follows an exponential decay with a minimum width of about 200–300 nm. Utilizing the exchange coupling between a Co layer with the FeNi layer through a Cu spacer, the authors studied the influence of interlayer coupling on the stripe-domain pattern. In a Co/Cu/(Fe/Ni)/Cu(001) structure, the Fe/Ni stripe orientation is found to be

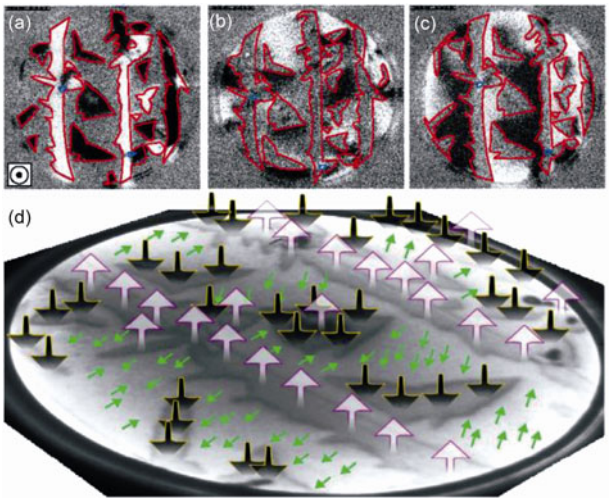

Figure 10 SPLEEM images of ~1.5 ML Co/Ru(0001). Images were taken at 110 K. Field of view is 2.8 μm and electron energy is 7 eV. (a)–(c) are images obtained with electron-polarization oriented: (a) out-of-plane; (b) in-plane and 13° off a compact direction; (c) in plane and 103° off a compact direction. 2-ML islands are framed in red (two small 3-ML islands are framed in blue). (d) LEEM image of the surface with the deduced magnetization direction indicated by arrows (black and white arrows mean out-of-plane magnetization; green arrows mean in-plane magnetization). Dark gray indicates 2-ML islands, light gray: 1-ML film. Taken from El Gabaly et al., [30]. Reprinted with permission from APS.

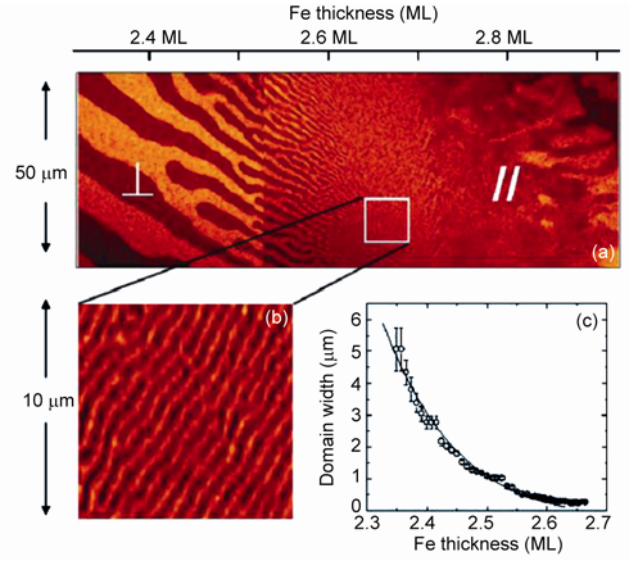

Figure 11 (a) PEEM image of the magnetic domains of Fe/Ni(5 ML)/Cu(001). The stripe domain width decreases as the Fe thickness increases towards to the SRT point at $t_{Fe} \approx 2.7$ ML. (b) A zoom-in image of the magnetic stripes in the box of (a). (c) Stripe domain width versus Fe film thickness. The solid line depicts the theoretical fitting. Taken from Wu et al. [55], Reprinted with permission from APS.

aligned with the Co in-plane magnetization, and the stripe domain width decreases exponentially with increasing the interlayer coupling between the Fe/Ni and Co films. Interestingly, an universal dependence of the stripe domain width on the magnetic anisotropy and on the interlayer coupling has been found by considering the stripes within an in-plane magnetic field [55] (see also refs. [49–52]).

4 Susceptibility studies of SRTs

Magnetic susceptibility, defined, generally, as the symmetric tensor $\chi = \mathrm{d}\boldsymbol{M} / \mathrm{d}\boldsymbol{H}$, where $\boldsymbol{M}$ is the magnetization and $\boldsymbol{H}$ is the applied magnetic field, has been widely used to explore critical phenomena in magnetic materials in the vicinity of the transition between ordered and disordered phases [1,59,60]. As $\boldsymbol{M}$ is usually the order parameter proper in such transitions, its singularity at the critical point is the strongest. In ferromagnetic transitions as those discussed in the present review, the transition temperature is traditionally denoted as the Curie temperature T_C. Right there, the system exhibits a distinct susceptibility peak (theoretically: a divergent one), which is readily detected via a field-modulation technique, for instance. In the context of ultrathin films, the magneto-optical Kerr effect (MOKE) has been used to probe χ [61]; the technique was extended to investigate the temperature-driven SRT [39,62].

The great advantage of using χ for the exploration of thickness-dependent SRTs was first demonstrated on the Co/Au(111) system, where a pronouncedly thickness-dependent χ was monitored *in situ* during film growth via MOKE measurements [63]. The theoretical description for the thickness-dependent χ for different types of SRT was streamlined very recently and applied consistently to provide unambiguous identification and quantification of the nature of this SRT [64]. Below, we will follow this work to, first, introduce the approach in general terms and, second, apply it to the purpose of conclusive comparison with most recent experimental results on the Co/Au(111) system.

4.1 Generalized χ representation for the thickness-driven SRT

In a susceptibility measurement, a small modulation field is applied. The results depend on the orientation of the modulation field. When the *ac* field is applied perpendicularly ($H_\perp$) to the sample plane, the free energy density can be written as:

$$f_A = \tilde{K}_1 \sin^2(\theta) + K_2 \sin^4(\theta) - \Delta HM \cos\theta, \qquad (8)$$

where ΔH is the *ac* modulation field. The last term is, in fact, the Zeeman term, but now with a very small amplitude. The system is in a single-domain state. In the ultrathin-film experiment, the experimental signal which is picked-up is sensitive to the total magnetic moment of the sample, which on its part is proportional to the thickness t on general dimensional grounds. It is thus both straightforward and advantageous to define the perpendicular and in-plane susceptibili-

ties by keeping the thickness dependence of the signal explicit:

$$\chi_{\perp} = \frac{\cos\theta_{\Delta H} - \cos\theta_{-\Delta H}}{2\Delta H} t; \tag{9}$$

$$\chi_{=} = \frac{\sin\theta_{\Delta H} - \sin\theta_{-\Delta H}}{2\Delta H} t. \tag{10}$$

In addition, dimensionless sets of anisotropy parameters are adopted $\{\tilde{K}_{1b} = -2,\ K_{1s}=1,\ K_{2b}=-1,\ K_{2S}=1\}$ or $\{\tilde{K}_{1b} = -1,\ K_{1s}=1,\ K_{2b}=-2,\ K_{2S}=1\}$ as representative of the two competing scenarios of a SRT via a canted or a coexistent state, respectively. Also, everywhere below in this section M is set to be 1 and ΔH equals 0.001.

The resulting perpendicular and in-plane susceptibilities for the canted-path and for the coexistent-phase scenarios are presented in Figures 12(a) and 12(b), respectively. For a crossover via the canted phase (Figure 12(a)), $\chi_{\perp}$ has a sharp peak at t_C=0.75 which corresponds to the critical thickness at the boundary between the canted and the in-plane state (cf. point C in Figure 1). The in-plane susceptibility has two distinct, even if weaker, peaks at t_B=0.5 and t_C=0.75. These represent the critical (crossover) points at the two boundaries of the canted state (cf. points B and C in Figure 1). However, near the SRT region, a multi-domain state is commonly found in experiment [23–25,55]. As a result, the perpendicular susceptibility $\chi_{\perp}$ remains in the normal direction while the contributions to the in-plane susceptibility $\chi_{=}$ are balanced by the domains with opposite horizontal components. Therefore, when the *ac* modulation field is applied perpendicularly to the sample plane, only the perpendicular susceptibility $\chi_{\perp}$ is detectable for a SRT via a canted state and it exhibits a single peak.

In the coexistent state, both in-plane and perpendicular domains can exist (hence, coexist as the name of the phase already suggests). However, the in-plane susceptibility is always zero during this evolution. Figure 12(b) displays the perpendicular susceptibility upon increasing the thickness around the SRT via a coexistent state. The situation can be conveniently resolved into two extreme or, if one prefers, pure situations when the magnetization is either fully in the perpendicular (upper line in Figure 12(b)) or fully in the in-plane state (lower line in Figure 12(b)). The measured susceptibility is a superposition of the pure situations. One finds that in each of the two cases a single peak at a distinct thickness emerges. Thus, the peak at t_F=0.6 corresponds to the emergence of nonzero in-plane magnetization (cf. point F in Figure 1), while the peak at t_G=1.0 matches the disappearance of vertical magnetization (point G in Figure 1). Generally, a double-peak susceptibility is to be expected in this part of the phase diagram for a range of overall "coexisting proportions" of in-plane to vertical magnetization.

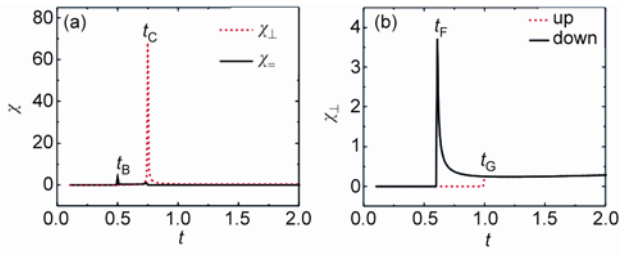

Figure 12 (a) Thickness dependence of the perpendicular (dashed line) and in-plane (solid line) susceptibilities around the SRT via a canted state. The ac modulation field is applied perpendicularly to the sample plane. (b) The perpendicular susceptibility close to a SRT via the coexistent state in a perpendicular ac modulation field. Upper line (dashed) and lower line (solid) represent the extreme (pure) cases when the magnetization in the coexistent region orients either fully perpendicularly or fully within the sample plane, respectively. Taken from Miao et al. [64]. Reprinted with permission from AIP.

When the *ac* field ($H_{=}$) is applied within the sample plane, the free energy density can be written as:

$$f_A = \tilde{K}_1 \sin^2(\theta) + K_2 \sin^4(\theta) + \Delta HM \sin\theta. \tag{11}$$

Similarly to the analysis of a perpendicular modulation field above, the perpendicular susceptibilities for both kinds of SRT can be neglected when the *ac* modulation field is in the plane of the sample. Figure 13(a) illustrates the in-plane susceptibility $\chi_{=}$ during a SRT via a canted state. The single peak at t_B=0.5 of $\chi_{=}$ corresponds to the transition from vertical to canted state. On the other hand, the thickness-dependent $\chi_{=}$ close to the SRT via a coexistent state displays two distinct peaks at t_F=0.6 and t_G=1.0, corresponding to the crossover points with the two boundaries of the coexistent region (Figure 13(b)).

Summarizing the most outstanding features of the two kinds of thickness-driven SRT, (i) for a SRT via the canted state, a single peak is expected regardless of whether the *ac* modulation field is vertical or in-plane; the peaks appear at different thicknesses, corresponding to the two critical points at each border of the canted phase; (ii) for a SRT via the coexistent phase, both susceptibilities in *ac* modulation fields, oriented within or perpendicularly to the plane of the sample, would typically exhibit two peaks. The two peaks appear at the same thicknesses for the modulation field ap-

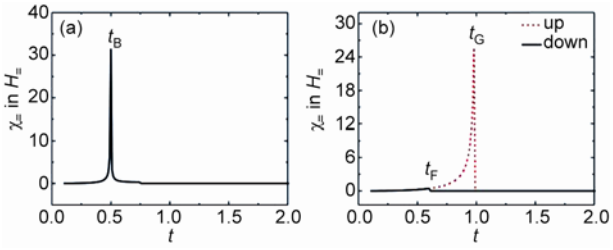

Figure 13 (a) Thickness dependence of the in-plane susceptibility close to the SRT via a canted state. The ac modulation field is applied within the sample plane. (b) The in-plane susceptibility around the SRT via a coexistent state in a horizontal modulation field. Upper line (dashed) and lower line (solid) have the same meaning as in Figure 12. Taken from Miao et al. [64]. Reprinted with permission from AIP.

plied in either perpendicular or in-plane directions. They represent two boundaries of the coexistent region. The possible singularities in the experimentally relevant cases have thus been conclusively 'fingerprinted' [64].

4.2 Application to the Co/Au(111) system

We now apply the general developments of the previous subsection to the analysis of the intensely studied Co/Au (111) system. For convenience of comparison, we plot the experimental and theoretical findings in one figure.

Thus, Figure 14(a) presents the susceptibility during Co growth. The cobalt films were grown by electron beam evaporation on a clean Au(111) surface at room temperature under UHV condition, and the typical rate was 0.3 MLs/min [63]. In order to minimize the influence of the transverse Kerr signal, *s*-polarized light was used [26,42]. Magnetic susceptibilities were obtained with *ac* magnetic fields oriented in both in-plane and perpendicular directions. The angles of incidence were 45° and 15° degrees for detecting the in-plane and vertical susceptibility, respectively. The in-plane and vertical *ac* modulation field was 0.12 mT and 0.05 mT, respectively [63]. No external field except the *ac* modulation field was applied for the cases in Figure 14(a). One can clearly recognize that the susceptibilities in vertical and in-plane *ac* field exhibit pronounced peaks around 4.38 MLs, and this is attributed to a SRT in progress. The thickness range is consistent with other reports in the literature [23,65]. At the same time, the polar signal shows an interesting behavior with χ exhibiting two peaks. However, apparently only a single broad peak is found with an in-plane *ac* field. The peak position coincides with that of one of the peaks in the vertical *ac* field.

The theoretical consideration from the previous subsection implies that the double peak is consistent with the SRT proceeding via a coexistent state. Hence, the experimental

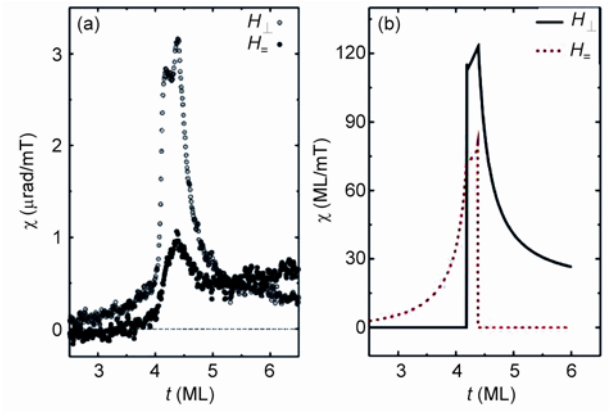

Figure 14 (a) Magnetic susceptibility measurements in different in-plane bias fields during the growth of Co/Au(111). The modulation field is applied along the normal direction. Taken from Pütter et al. [63]. Reprinted with permission from APS. (b) Calculated magnetic susceptibilities according to the experimental conditions shown in (a). Taken from Miao et al. [64]. Reprinted with permission from AIP.

double-peak phenomenon provides direct evidence for the thickness-driven SRT in Co/Au(111) proceeding via a coexistent state. The fact that the peak position in longitudinal susceptibility at 4.39 MLs is coincident with one of the peak positions in the polar susceptibility provides additional evidence for a transition via a coexistent state. The two peaks in the polar susceptibility represent the two borders of the coexistent region (cf. point F and G in Figure 1). The broad peak in the longitudinal susceptibility is most likely a superposition of these peaks. Within the setting, described above, we can then employ the conditions for the peaks at F and G as given in eq. (7).

For cobalt deposited on Au(111), one monolayer corresponds to about two Angstrom: 1 ML $\approx$ 0.2 nm [13]. Furthermore, we take the bulk values for *hcp* cobalt at room temperature, which are K_{1b}=4.1×10^5 J/m^3, K_{2b}=1.5×10^5 J/m^3, and M=1.4×10^6 A/m [3]. Solving eq. (7), one finds the surface/interface anisotropy constants to be K_{1s}=7.21×10^{-4} J/m^2 and K_{2s}=–1.43×10^{-4} J/m^2 for the Co/Au(111) system. The obtained values agree reasonably well with the values, derived by other authors [3,25,66].

For simplicity, the in-plane magnetic magnetization is assumed to increase linearly with the film thickness in the coexistent region. With the experimental parameters, the susceptibility dependence on the film thickness has been calculated and presented in Figure 14(b). For the purpose of ease of comparison, the susceptibility is given in units of MLs/mT. If a precise quantitative comparison is pursued, the signal should be multiplied by the sensitivity of the specific experimental setup which could also vary with the different geometries, used for the susceptibility probe. The calculated susceptibility in a perpendicular *ac* modulation field exhibits two peaks at 4.19 MLs and 4.39 MLs, while only one broad peak at 4.39 MLs is observed in an in-plane field. The main features of the calculations agree surprisingly well with the experimental findings despite the simple linear assumption above.

Theoretically, Millev et al. predicted that the presence of external magnetic field would modify the phase diagram and change the critical thicknesses where the SRT occurs [32]. For the Co/Au(111) system, the in-plane field will shift the SRT to a lower range of thicknesses. Figure 15(a) shows the experimental results for Co/Au(111) system under different external bias fields, namely, 50.8 mT and 111.3 mT, applied along the in-plane direction. Indeed, the SRT shifts to lower thickness when in-plane *dc* fields are applied in good agreement with the theoretical expectation [32]. Besides, the double-peak phenomenon disappears with increasing the *dc* magnetic field (see Figure 15).

With an additional finite and constant (as opposed to the small modulational) Zeeman energy term, the model discussed in the previous section can also be extended to determine the influence of external fields on the thickness-dependent susceptibility throughout the SRT. In the calculations, the in-plane magnetization is again assumed to in-

crease linearly with the film thickness during the transition. The results are shown in Figure 15(b). With an increasing in-plane *dc* bias field, the SRT thickness shifts to lower thicknesses with respect to the zero-field configuration. Both susceptibility curves, taken under 50.8 mT and 111.3 mT, respectively, exhibit two peaks which are closer now. The separation between the two peaks decreases and the peak intensities increase with increasing the bias field. The calculations nicely reflect the experimental findings. The discrepancy in peak numbers (two peaks in calculations and one peak in experiment) may be the outcome of the linear assumption we adopted for the magnetization constitution in the SRT region, since the applied *dc* magnetic field may influence the proportion of the contributions from in-plane and vertical magnetization in a more subtle, and in any case nonlinear way. When the proportion is slightly modified, the peak at t_F can disappear while the peak at t_G is less sensitive.

To facilitate quantitative use and comparison, the calculated critical film thicknesses t_F and t_G in different external fields together with the experimental values (last column) are collected in Table 1 [64]. The small discrepancy may derive from the experimental error margin (0.07 MLs) [63] or from the assumptions adopted for the calculation (for instance, the neglected in-plane anisotropy). When the

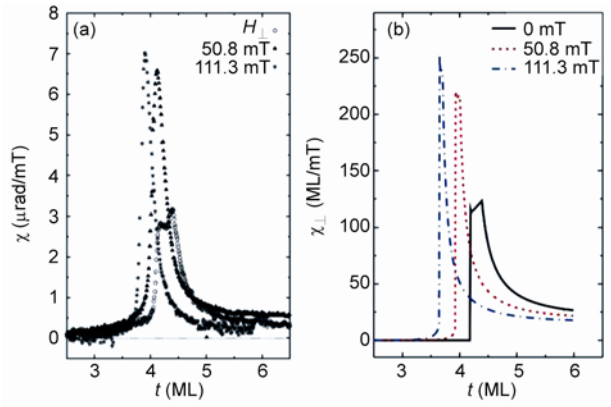

Figure 15 (a) Magnetic susceptibility measurements during the growth of Co/Au(111) in different in-plane bias fields. The modulation field is applied along the normal direction. Taken from Pütter et al. [63]. Reprinted with permission from APS. (b) Calculated magnetic susceptibilities according to the experimental conditions shown in (a). Taken from Miao et al. [64]. Reprinted with permission from AIP.

Table 1 Comparison table of several critical thicknesses under different bias fields. t_F and t_G represent the two critical thicknesses at the boundaries of the coexistent region. Calculated values for t_F and t_G are listed for both cases without in-plane anisotropy and with bulk in-plane anisotropy included, respectively. The last column records the experimental results from ref. [63]. Taken from Miao et al. [64] Reprinted with permission form AIP

Horizontal field	Without in-plane anisotropy		With bulk in-plane anisotropy		Exp. (ML)
	t_F (ML)	t_G (ML)	t_F (ML)	t_G (ML)	
50.8 mT	3.91	4.01	4.00	4.12	4.11
111.3 mT	3.64	3.71	3.81	3.86	3.90

six-fold bulk in-plane anisotropy of 6.0×10^3 J/m^3 [30] at room temperature is included, a better agreement with the experimental values is achieved. The peak positions at t_G are shifted to 4.12 MLs and 3.86 MLs in 50.8 mT and 111.3 mT bias fields, respectively (see Table 1). Working in reverse order and utilizing the peak position shift with field, one could estimate the in-plane anisotropy constant [64].

5 Summary

In the article, we reviewed recent studies by means of different modern approaches to thickness-driven spin reorientation transitions in ultrathin films. Sound qualitative and quantitative grip on such transitions was based on a phenomenological thermodynamic description, which provides the generic phase diagrams in anisotropy space for all possible types of SRT, with or without applied magnetic field Three principal approaches, including the macroscopic methods (hysteresis-loop analysis, susceptibility measurements) and microscopic ones (magnetic-domain studies) were introduced and illustrated on the examples of a few relevant experimental systems, where these methods proved to be most appropriate and, in fact, indispensable. All along, we traced out two intimately interrelated problems, (i) how to determine in a reliable and consistent fashion whether the transitions proceed via a canted state or via a coexistence one, and (ii) how to deduce the most important material parameters in any ultrathin-film SRT, namely, the surface (interface) magnetic anisotropy constants. A reference case in point was the ultrathin system Co/Au(111), where we established conclusively that the thickness-driven SRT proceeds along a path through the state of coexisting phases.

Needless to say, having only a few atomic layers along one of its dimensions an ultrathin film qualifies as a nanoscale system in terms of physical characteristic lengths [58,67,68] but also in terms of formal definitions like those adopted for the US National Nanotechnology Initiative [http://www.nano.gov]. Optimistically, such films may be viewed as the simplest finite-size systems. Even if one stays with only thickness-driven SRTs and their concomitant thickness-dependent domain structures, there are many unresolved questions to explore. Rigorous quasi-2d analysis has already shed light on the 'mathematically ultrathin' limit t -> 0, which turns out to be surprisingly difficult to handle [69]. Not surprisingly, as soon as an additional dimension is allowed to shrink an entirely new set of complications arises as can be seen again in very recent rigorous developments for the micromagnetic behavior of soft disks for very small aspect ratios [67]. In the spirit of micromagnetism [11,58,68], the just-mentioned analyses assume the validity of the continuum description while the grainy atomistic structure of real ultrathin films is bound to affect the formal limiting process, on one hand, and the actual experiments on SRTs, on the other. Progress in the understanding

of the finite-size corrections to the continuum micromagnetic picture has begun some time ago (see, e.g., [70,71]), but the direct implications for SRTs in doubly finite (ultrathin and laterally constrained) films have only been singled out and quantified very recently [72–74]. These studies were theoretical and, in addition, mostly heavily supported by numerical computation. We believe that experimental advances in detecting and making use of finite-size effects of the above type in systems with SRTs would naturally follow. So far as the critical behavior proper of such systems is concerned, there is no doubt that the ideas of finite-size scaling analysis would provide the needed general framework [75], just like Landau theory of phase transitions underpins the thermodynamic analysis, presented earlier in this review. Susceptibility measurements, similar to those discussed in the present work, would naturally be the weapon of choice. Of course, there are many other finite-size magnetic systems that have been of prime interest such as magnetic nanowires [76], magnetic dots, and arrays thereof [77]. Clearly, it is not possible to even only enumerate the essential developments in this field. In short, there is much to be expected from thickness-driven, thickness-related, or more generally finite-size spin-reorientation transitions.

This work was supported by the State Key Programme for Basic Research of China (Grant No. 2010CB923401), National Natural Science Foundation of China (Grant Nos. 10834001, 10974087 and 11023002), Natural Science Foundation of Jiangsu (Grant No. BK2012300), and PAPD. YTM gratefully acknowledges the warm hospitality of the National Laboratory of Solid State Microstructures and the Department of Physics during his visit at Nanjing University in September 2012.

1 Chikazumi S. Physics of Ferromagnetism. New York: Oxford University press Inc.,1997
2 Cullity B D. Introduction to Magnetic Materials. Reading, MA: Addison-Wesley Pub Co,1972
3 Bland J A C, Heinrich B. Ultrathin Magnetic Structures I: An Introduction to the Electronic, Magnetic and Structural Properties. Berlin: Springer, 2005
4 Baibich M N, Broto J M, Fert A, et al. Giant magnetoresistance of (001)Fe/(001)Cr magnetic superlattices. Phys Rev Lett, 1988, 61(21): 2472–2475
5 Binasch G, Grünberg P, Saurenbach F, et al. Enhanced magnetoresistance in layered magnetic structures with antiferromagnetic interlayer exchange. Phys Rev B, 1989, 39(7): 4828–4830
6 Wolf S A, Awschalom D D, Buhrman R A, et al. Spintronics: A spin-based electronics vision for the future. Science, 2001, 294(5546): 1488–1495
7 Aktas B, Tagirov L, Mikailov F. Magnetic Nanostructures. Berlin: Springer, 2007
8 Michael F. Ferromagnetic resonance of ultrathin metallic layers. Rep Prog Phys, 1998, 61(7): 755–826
9 Sander D. The magnetic anisotropy and spin reorientation of nanostructures and nanoscale films. J Phys-Condens Matter, 2004, 16(20): R603–R606
10 Landau L D, Lifshitz E M. Electrodynamics of Continuous Media. Transl from the Russian by Sykes J B and Bell J S. Oxford: Pergamon Press,1963
11 Brown W F. Magnetostatic Principles in Ferromagnetism. Amsterdam: North-Holland Pub Co, 1962
12 Bertram H N, Williams M. SNR and density limit estimates: a comparison of longitudinal and perpendicular recording. IEEE Trans Magn, 2000, 36(1): 4–9
13 Cagnon L, Devolder T, Cortes R, et al. Enhanced interface perpendicular magnetic anisotropy in electrodeposited Co/Au(111) layers. Phys Rev B, 2001, 63(10): 104419
14 Ikeda S, Miura K, Yamamoto H, et al. A perpendicular-anisotropy CoFeB-MgO magnetic tunnel junction. Nat Mater, 2010, 9(9): 721–724
15 Néel L. Anisotropie magnétique superficielle et surstructures dorientation. J Phys Radium, 1954, 15(4): 225–239
16 Bruno P. Magnetic surface anisotropy of cobalt and surface roughness effects within Neel's model. J Phys F-Metal Phys, 1988, 18(6): 1291–1298
17 Daalderop G H O, Kelly P J, Schuurmans M F H. First-principles calculation of the magnetic anisotropy energy of $(Co)_n/(X)_m$ multilayers. Phys Rev B, 1990, 42(11): 7270–7273
18 Millev Y T, Skomski R, Kirschner J. Higher-order and next-nearest-neighbor Néel anisotropies. Phys Rev B, 1998, 58(10): 6305–6315
19 Liu C, Moog E R, Bader S D. Polar Kerr-effect observation of perpendicular surface anisotropy for ultrathin fcc Fe grown on Cu(100). Phys Rev Lett, 1988, 60(23): 2422–2425
20 Koon N C, Jonker B T, Volkening F A, et al. Direct evidence for perpendicular spin orientations and enhanced hyperfine fields in ultrathin Fe(100) films on Ag(100). Phys Rev Lett, 1987, 59(21): 2463–2466
21 Qiu Z Q, Pearson J, Bader S D. Asymmetry of the spin reorientation transition in ultrathin Fe films and wedges grown on Ag(100). Phys Rev Lett, 1993, 70(7): 1006–1009
22 Wilgocka-Ślęzak D, Freindl K, Kozioł A, et al. Thickness-driven polar spin reorientation transition in ultrathin Fe/Au(001) films. Phys Rev B, 2010, 81(6): 064421
23 Allenspach R, Stampanoni M, Bischof A. Magnetic domains in thin epitaxial Co/Au(111) films. Phys Rev Lett, 1990, 65(26): 3344–3347
24 Speckmann M, Oepen H P, Ibach H. Magnetic domain structures in ultrathin Co/Au(111): On the influence of film morphology. Phys Rev Lett, 1995, 75(10): 2035–2038
25 Oepen H P, Speckmann M, Millev Y, et al. Unified approach to thickness-driven magnetic reorientation transitions. Phys Rev B, 1997, 55(5): 2752–2755
26 Ding H F, Pütter S, Oepen H P, et al. Spin-reorientation transition in thin films studied by the component-resolved Kerr effect. Phys Rev B, 2001, 63(13): 134425
27 Sellmann R, Fritzsche H, Maletta H, et al. Spin-reorientation transition and magnetic phase diagrams of thin epitaxial Au(111)/Co films with W and Au overlayers. Phys Rev B, 2001, 64(5): 054418
28 Schulz B, Baberschke K. Crossover from in-plane to perpendicular magnetization in ultrathin Ni/Cu(001) films. Phys Rev B, 1994, 50(18): 13467–13471
29 O'brien W L, Droubay T, Tonner B P. Transitions in the direction of magnetism in Ni/Cu(001) ultrathin films and the effects of capping layers. Phys Rev B, 1996, 54(13): 9297–9303
30 El Gabaly F, Gallego S, Muñoz C, et al. Imaging spin-reorientation transitions in consecutive atomic Co layers on Ru(0001). Phys Rev Lett, 2006, 96(14): 147202
31 Millev Y, Kirschner J. Reorientation transitions in ultrathin ferromagnetic films by thickness- and temperature-driven anisotropy flows. Phys Rev B, 1996, 54(6): 4137–4145
32 Millev Y T, Oepen H P, Kirschner J. Influence of external field on spin reorientation transitions in uniaxial ferromagnets I General analysis for bulk and thin-film systems. Phys Rev B, 1998, 57(10): 5837–5847
33 Gradmann U, Müller J. Flat Ferromagnetic, epitaxial 48Ni/52Fe(111) films of few atomic layers. Physica Status Solidi B, 1968, 27(1): 313–324
34 Dzyaloshinsky I. A thermodynamic theory of "weak" ferromagnetism of antiferromagnetics. J Phys Chem Solids, 1958, 4(4): 241–255
35 Moriya T. Anisotropic superexchange interaction and weak ferromagnetism. Phys Rev, 1960, 120(1): 91–98

36 Popov A P, Skorodumova N V, Eriksson O. Phenomenological model of the magnetic states of ferromagnetic film with competing surface and bulk anisotropies. Phys Rev B, 2008, 77(1): 014415
37 Millev Y T, Oepen H P, Kirschner J. Phase boundaries of a uniaxial system in an applied field of arbitrary direction. J Phys D-Appl Phys, 1999, 32(20): 2599–2604
38 Millev Y T, Oepen H P, Kirschner J. Influence of external fields on spin reorientation transitions in uniaxial ferromagnets II Ultrathin ferromagnetic films. Phys Rev B, 1998, 57(10): 5848–5859
39 Garreau G, Beaurepaire E, Ounadjela K, et al. Spin-reorientation transition in ultrathin Tb/Co films. Phys Rev B, 1996, 53(3): 1083–1086
40 Bader S D. Surface magneto-optic Kerr effec. J Magn Magn Matter, 1991, 100(1-3): 440–454
41 Qiu Z Q, Bader S D. Surface magneto-optic Kerr effect (SMOKE). J Magn Magn Matter, 1999, 200(1-3): 664–678
42 Ding H F, Pütter S, Oepen H P, et al. Experimental method for separating longitudinal and polar Kerr signals. J Magn Magn Matter, 2000, 212(1-2): 5–11
43 Heinrich B, Bland J A C. Ultrathin Magnetic Structures II: Measurement Techniques and Novel Magnetic Properties. Berlin, Heidelberg: Springer, 2005
44 Rougemaille N, Schmid A K. Magnetic imaging with spin-polarized low-energy electron microscopy. Eur Phys J-Appl Phys, 2010, 50(02): 20101
45 Anders S, Padmore H A, Duarte R M, et al. Photoemission electron microscope for the study of magnetic materials. Rev Sci Instruments, 1999, 70(10): 3973–3981
46 Hopster H, Oepen H P. Magnetic Microscopy of Nanostructures. New York: Springer, 2005
47 Ibach H. Electron Spectroscopy for Surface Analysis. Berlin: Springer, 1977
48 Kirschner J. Polarized Electrons at Surfaces. New York: Springer, 1985
49 Kaplan B, Gehring G A. The domain structure in ultrathin magnetic films. J Magn Magn Matter, 1993, 128(1-2): 111–116
50 Rowlands G. Magnetostatic energy calculations for domains in rectangular slabs. J Magn Magn Matter, 1994, 136(3): 284–286
51 Millev Y. Bose-Einstein integrals and domain morphology in ultrathin ferromagnetic films with perpendicular magnetization. J Phys-Condens Matter, 1996, 8(20): 3671–3676
52 Braun A. Quantitative model for anisotropy and reorientation thickness of the magnetic moment in thin epitaxially strained metal films. Physica B-Condensed Matter, 2006, 373(2): 346–354
53 Frömter R, Stillrich H, Menk C, et al. Imaging the cone state of the spin reorientation transition. Phys Rev Lett, 2008, 100(20): 207202
54 Vedmedenko E Y, Oepen H P, Kirschner J. Microstructure of the spin reorientation transition in second-order approximation of magnetic anisotropy. Phys Rev B, 2002, 66(21): 214401
55 Wu Y Z, Won C, Scholl A, et al. Magnetic stripe domains in coupled magnetic sandwiches. Phys Rev Lett, 2004, 93(11): 117205
56 Allenspach R, Bischof A. Magnetization direction switching in Fe/Cu(100) epitaxial films: Temperature and thickness dependence. Phys Rev Lett, 1992, 69(23): 3385–3388
57 Vaterlaus A, Stamm C, Maier U, et al. Two-step disordering of perpendicularly magnetized ultrathin films. Phys Rev Lett, 2000, 84(10): 2247–2250
58 Hubert A, Schaefer R. Magnetic Domains. Berlin: Springer,1998
59 Coey J M D. Magnetism and Magnetic Materials. Cambridge: Cambridge University Press, 2010
60 Uzunov D I. Introduction to the Theory of Critical Phenomena: Mean Field, Fluctuations and Renormalization. Singapore: World Scientific, 2010
61 Berger A, Knappmann S, Oepen H P. Magneto-optical Kerr effect study of ac susceptibilities in ultrathin cobalt films. J Appl Phys, 1994, 75(10): 5598–5600
62 Arnold C S, Pappas D P, Popov A P. Second- and first-order phase transitions in the magnetic reorientation of ultrathin Fe on Gd. Phys Rev Lett, 1999, 83(16): 3305–3308
63 Pütter S, Ding H F, Millev Y T, et al. Magnetic susceptibility: An easy approach to the spin-reorientation transition. Phys Rev B, 2001, 64(9): 092409
64 Miao B F, Sun L, You B, et al. Probe the spin-reorientation transition with magnetic susceptibility—a theoretical analysis. J Appl Phys, 2011, 109(11): 113902
65 Oepen H P, Millev Y T, Kirschner J. The reorientation transition in Co/Au(111). J Appl Phys, 1997, 81(8): 5044–5046
66 Fritzsche H, Kohlhepp J, Gradmann U. Second- and fourth-order magnetic surface anisotropy of Co(0001)-based interfaces. J Magn Magn Matter, 1995, 148(1-2): 154–155
67 Kohn R V, Slastikov V V. Another thin-film limit of micromagnetics. Arch Rational Mech Anal, 2005, 178(2): 227–245
68 Brown W F. Micromagnetics. New York, London: Interscience Publishers, 1963
69 Desimone A, Kohn R V, Müller S, et al. Two–dimensional modelling of soft ferromagnetic films. Proc R Soc London Ser A-Math Phys Eng Sci, 2001, 457(2016): 2983–2991
70 Christensen P H, Mørup S. On the magnetic dipole fields at surface atoms. J Magn Magn Matter, 1983, 35(1-3): 130–132
71 Draaisma H J G, De Jonge W J M. Surface and volume anisotropy from dipole-dipole interactions in ultrathin ferromagnetic films. J Appl Phys, 1988, 64(7): 3610–3613
72 Vedmedenko E Y, Oepen H P, Kirschner J. Size-dependent magnetic properties in nanoplatelets. J Magn Magn Matter, 2003, 256(1-3): 237–242
73 Millev Y T, Vedmedenko E, Oepen H P. Dipolar magnetic anisotropy energy of laterally confined ultrathin ferromagnets: multiplicative separation of discrete and continuum contributions. J Phys D-Appl Phys, 2003, 36(23): 2945–2949
74 Vedmedenko E Y. Influence of the lattice discreteness on magnetic ordering in nanostructures and nanoarrays. Physica Status Solidi (b), 2007, 244(4): 1133–1165
75 Barber M N. Finite-size Scaling. London: Academic Press, 1983
76 Parkin S S P, Hayashi M, Thomas L. Magnetic domain-wall racetrack memory. Science, 2008, 320(5873): 190–194
77 Fruchart O, Thiaville A. Magnetism in reduced dimensions. Comptes Rendus Physique, 2005, 6(9): 921–933